Chiral tunneling modulated by a time-periodic potential on the surface states of a topological insulator

Yuan Li[1,2], Mansoor B. A. Jalil[2], S. G. Tan[2], W. Zhao[1], R. Bai[3] & G. H. Zhou[4]

[1]Department of Physics, Hangzhou Dianzi University, Hangzhou, Zhejiang 310018, China, [2]Department of Electronic and Computer Engineering, Information Storage Materials Laboratory, National University of Singapore, 1 Engineering Drive 3, Singapore 117576, Singapore, [3]Center for Integrated Spintronic Devices (CISD), Hangzhou Dianzi University, Hangzhou, Zhejiang 310018, China and, [4]Department of Physics and Key Laboratory for Low-Dimensional Quantum Structures and Manipulation (Ministry of Education), Hunan Normal University, Changsha 410081, China.

Time-periodic perturbation can be used to modify the transport properties of the surface states of topological insulators, specifically their chiral tunneling property. Using the scattering matrix method, we study the tunneling transmission of the surface states of a topological insulator under the influence of a time-dependent potential and finite gate bias voltage. It is found that perfect transmission is obtained for electrons which are injected normally into the time-periodic potential region in the absence of any bias voltage. However, this signature of Klein tunneling is destroyed when a bias voltage is applied, with the transmission probability of normally incident electrons decreasing with increasing gate bias voltage. Likewise, the overall conductance of the system decreases significantly when a gate bias voltage is applied. The characteristic left-handed helicity of the transmitted spin polarization is also broken by the finite gate bias voltage. In addition, the time-dependent potential modifies the large-angle transmission profile, which exhibits an oscillatory or resonance-like behavior. Finally, time-dependent transport modes (with oscillating potential in the THz frequency) can result in enhanced overall conductance, irrespective of the presence or absence of the gate bias voltage.

Topological insulators (TI) form a new class of quantum matter possessing insulating bulk and metallic edge or surface states[1,2]. The surface states of TIs have an odd number of massless Dirac cones[3], which are protected against time-reversal-invariant perturbations such as non-magnetic impurities, defects, and reconstruction. This promising characteristic motivates significant interest in the fundamental physics of transport in TIs[4–9]. Due to the robustness of the surface states against time-reversal symmetric perturbations, TIs are expected to be good candidates for the design of spintronics devices[10]. TI is also a good candidate for fault-tolerant quantum computing[11] because of the formation of Majorana bound state induced by the superconducting proximity effect[12].

To realize the practical TI-based devices, one major task is to effectively control and adjust the transport properties of the surface states. Correspondingly, some interesting effects, such as finite-size effects[13,14], ferromagnetic coupling[15,16], and quantum confinement[17,18] have been utilized to achieve this goal. In semiconductors one can confine electrons quantum mechanically using electrostatic barriers, e.g. a quantum well. However, such electrostatic barriers cannot provide electron confinement in graphene and TI systems, due to chiral tunneling of Dirac fermions, a phenomenon which has been extensively studied recently[19–25]. The chirality of electron's wavefunction in graphene gives rise to perfect quantum tunneling for electrons incident in the normal direction of a potential barrier[23]. The chiral nature of Dirac fermions also suppresses the backscattering of quasiparticles leading to high charge carrier mobility, which can be utilized in some novel nanodevices[26,27]. Similarly, the surface states of TIs can also mimic Dirac fermions in quantum electrodynamics (QED). Naturally, it is meaningful to study the chiral tunneling of quasiparticles when a potential barrier is applied to the topological surface states. In recent years, much attention is paid to optical response of the topological surface states[28–33]. Applying a time-dependent perturbation can provide an alternative and efficient way to control spectrum and transport properties, e.g., inducing a topological state in a semiconductor quantum well[34] and a conventional insulator[35], resulting in Floquet-Bloch bands due to the hybridization of bulk states and topological surface states[36].
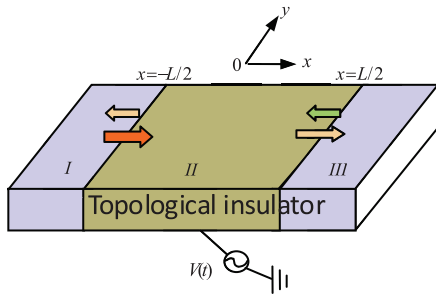
Figure 1 | Schematic of the conducting channel with time-periodic potential comprising of topological surface states.

However, relatively few studies have been conducted on the chiral tunneling of surface states under the influence of a time-dependent potential, or under nonequilibrium condition, i.e., in the presence of a gate bias voltage.

In this work, we consider a conducting channel consisting of topological surface states influenced by a time-periodic potential, shown schematically in Fig. 1. It is found that in general, a time-dependent potential modifies the large-angle transmission of the device, which exhibits oscillatory or resonance-like behaviors. On the other hand, the presence of a gate bias voltage can significantly affect the transmission probability of normally-incident electrons, and destroys the perfect transmission for normally-incident electrons, which is a signature of the Klein tunneling effect[23]. The characteristic left-handed helicity of the transmitted spin polarization is also destroyed by the finite gate bias voltage. However, the zero-angle spin polarization is robust against the time-dependent potential and the gate bias voltage. Finally, by applying the scattering matrix method, we numerically study the amplitude and frequency dependence on the transmission probability, and describe the time-dependent response of the systems conductance in the presence or absence of a gate bias voltage.

This paper is organized as follows. In section Model and formulation, we consider the Dirac equation governing the topological surface states of the system in the presence of the time-periodic potential in the central region and a gate bias voltage across the left and right portions of the conducting channel. By solving the Dirac equation, we obtain the analytic solution of the time-dependent wavefunction. We employ the scattering matrix method to calculate the transmission probability and the device conductance. In section Numerical results and discussion, we analyze the dependence of the transmission probability on the electron injection-angle and the frequency dependence of both the transmission probability and the overall conductance. We summarize the main results in section Summary.

Model and formulation

In this section, we investigate the transport property of a conducting channel proposed of topological surface states, as illustrated in Fig. 1, modulated by a time-dependent potential, which arises from a small ac signal $V(t)$ applied to the gate voltage in the central region.

At low energies, the surface states can be described by the effective Hamiltonian[3]

$$H = v_F(p_y \sigma_x - p_x \sigma_y), \quad (1)$$

where v_F is the velocity of the surface states, $v_F \simeq 5 \times 10^5 \text{m/s}$ for the typical topological insulator Bi_2Se_3. The wavefunction of the time-dependent system satisfies the following Dirac equation

$$-i\hbar v_F \begin{pmatrix} 0 & \partial_y + i\partial_x \\ \partial_y - i\partial_x & 0 \end{pmatrix} \psi_i - \mu(x)\psi_i = i\hbar \partial_t \psi_i, \quad (2)$$

where $i = 1, 2, 3$ are the notations of three different regions, $\psi_i = (\psi_\uparrow, \psi_\downarrow)_i^T$ is the two-component wavefunction with $\uparrow, \downarrow$ being spin indexes. The potential function $\mu(x)$ is written as

$$\mu(x) = \begin{cases} \mu_L, & x < -L/2, \\ -u_0 \cos(\omega t), & -L/2 \le x \le L/2, \\ \mu_R, & x > L/2. \end{cases} \quad (3)$$

This potential profile of the conducting channel can be envisaged by applying top-gate and back-gate voltages[37–40], where $\mu_{\alpha=L,R}$ describe the relative shift of Dirac points of region *I* and *III* with respect to region *II*, $V = (\mu_L - \mu_R)/e$ is defined as the gate bias voltage, and u_0 and ω are the amplitude and frequency of the time-dependent potential.

Firstly, we try to find the solution of Eq. (2) for the central region. The wavefunction can be constructed as[41]

$$\psi_2(\mathbf{r},t) = \psi_{20}(\mathbf{r})e^{-i(\varepsilon\omega t + u_0 \sin \omega t)/\hbar\omega}$$
$$= \sum_{m=-\infty}^{\infty} J_m\left(\frac{u_0}{\hbar\omega}\right)\psi_{20}(\mathbf{r})e^{-i(\varepsilon + m\hbar\omega)t/\hbar}, \quad (4)$$

where $\psi_{20}(\mathbf{r})$ is also a two-component wavefunction, whose explicit form is given below, and J_m refers to the mth-order Bessel function. Substituting Eq. (4) into Eq. (2), we can obtain the equation satisfied by $\psi_{20}(\mathbf{r})$

$$-i\hbar v_F \begin{pmatrix} 0 & \partial_y + i\partial_x \\ \partial_y - i\partial_x & 0 \end{pmatrix} \psi_{20}(\mathbf{r}) = \varepsilon\psi_{20}(\mathbf{r}). \quad (5)$$

Thus the solution of the two-component wavefunction can be expressed as

$$\psi_{20,\pm}(\mathbf{r}) = \frac{1}{\sqrt{2}} \begin{pmatrix} \gamma e^{i(\frac{\pi}{2} - \theta)} \\ 1 \end{pmatrix} e^{i(k_x x + k_y y)}, \quad (6)$$

where $k = \sqrt{k_x^2 + k_y^2}$ is the amplitude of the wave vector, $\theta = \arcsin(\hbar v_F k_y/|\varepsilon|)$, $k_x(\varepsilon) = |\varepsilon|\cos\theta/(\hbar v_F)$, and $\gamma(\varepsilon) = \text{sgn}(\varepsilon) = \pm 1$ corresponding to electronlike and holelike cases, respectively. Correspondingly, the wavefunctions $\psi_{1,3}(\mathbf{r}, t)$, in the regions $|x| > L/2$, obey similar formulas to Eq. (5), and the solution of which can be written as

$$\psi_{1,3,\pm}(\mathbf{r},t) = \frac{1}{\sqrt{2}} \begin{pmatrix} \gamma_0 e^{i(\frac{\pi}{2} - \theta_0)} \\ 1 \end{pmatrix} e^{i(q_x x + q_y y)} e^{-i\varepsilon t/\hbar}, \quad (7)$$

where $q = \sqrt{q_x^2 + q_y^2}$ is also the amplitude of the wave vector, $\theta_{0,\alpha} = \arcsin(\hbar v_F q_y/|\varepsilon + \mu_a|)$, $q_{x,a}(\varepsilon) = |\varepsilon + \mu_a|\cos\theta_{0,a}/(\hbar v_F)$, and $\gamma_{0,\alpha}(\varepsilon) = \text{sgn}(\varepsilon + \mu_\alpha) = \pm 1$.

Thus for a charge particle with an energy ε which is injected from region *I* into the center region, the wavefunctions in the three regions can be written as

$$\psi_1(\mathbf{r},t) = \frac{e^{-i\varepsilon t/\hbar}}{\sqrt{2}}\left\{ \begin{pmatrix} \gamma_{0,L}(\varepsilon)e^{i(\frac{\pi}{2} - \theta_{0,L})} \\ 1 \end{pmatrix} e^{i[q_{x,L}(\varepsilon)x + q_{y0}y]} + \sum_{m=-\infty}^{\infty} r_m(\varepsilon) \right.$$
$$\times \begin{pmatrix} \gamma_{0,L}(\varepsilon + m\hbar\omega)e^{i(\theta_{(m,0),L} - \frac{\pi}{2})} \\ 1 \end{pmatrix}$$
$$\left. \times e^{i[-q_{x,L}(\varepsilon + m\hbar\omega)x + q_{y0}y]}e^{-im\omega t}\right\}, x < -L/2, \quad (8)$$

2

$$\psi_2(\mathbf{r},t) = \sum_{m',n} J_n\left(\frac{u_0}{\hbar\omega}\right) e^{-i[\varepsilon+(m'+n)\hbar\omega]t/\hbar} \frac{e^{iq_{y0}y}}{\sqrt{2}}\Big\{A(m')$$

$$\begin{pmatrix} \gamma(\varepsilon+m'\hbar\omega)e^{i\left(\frac{\pi}{2}-\theta\right)} \\ 1 \end{pmatrix} e^{ik_x(\varepsilon+m'\hbar\omega)x} \qquad (9)$$

$$+ B(m')\begin{pmatrix} \gamma(\varepsilon+m'\hbar\omega)e^{i\left(\theta-\frac{\pi}{2}\right)} \\ 1 \end{pmatrix} e^{-ik_x(\varepsilon+m'\hbar\omega)x}\Big\},$$

$$-L/2 \le x \le L/2,$$

$$\psi_3(\mathbf{r},t) = \frac{e^{-i\varepsilon t/\hbar}}{\sqrt{2}}\Big\{\sum_{m=-\infty}^{\infty} t_m(\varepsilon)\begin{pmatrix} \gamma_{0,R}(\varepsilon+m\hbar\omega)e^{i\left(\frac{\pi}{2}-\theta_{(m,0),R}\right)} \\ 1 \end{pmatrix}$$

$$e^{i[q_{x,R}(\varepsilon+m\hbar\omega)x+q_{y0}y]}e^{-im\omega t}\Big\}, \qquad (10)$$

$$x > L/2.$$

Imposing the boundary conditions for the wavefunctions $\psi_i(\mathbf{r}, t)$, which must be continuous at the interfaces of $x = \pm L/2$, we can obtain the equations relating $A(m')$ and $B(m')$ utilizing the orthogonality of $\{e^{-im\omega t}\}$. After some algebra, we obtain the coefficients $A(m')$ and $B(m')$, and substitute them into the following equation to calculate the transmission coefficients

$$t_m(\varepsilon) = e^{-iq_{xR}(\varepsilon+m\hbar\omega)L/2} \sum_{m'} \Big[A(m')e^{ik_x(\varepsilon+m'\hbar\omega)L/2}$$

$$+ B(m')e^{-ik_x(\varepsilon+m'\hbar\omega)L/2} \Big] J_{m-m'}\left(\frac{u_0}{\hbar\omega}\right). \qquad (11)$$

After these quantities are obtained, we can study the quantum transport property of the considered system using the scattering matrix method[42–44]. Correspondingly, we can obtain the total transmission probability

$$T = \sum_m \frac{q_{xR}(\varepsilon+m\hbar\omega)}{q_{xL}(\varepsilon)}|t_m(\varepsilon)|^2. \qquad (12)$$

Consider an electron incident from region I with a fixed Fermi energy E_F. The electron can be injected into the central region at various incidence angle θ, associated with different y-component wavevector q_{y0}. We can calculate the transmission probability for a fixed q_{y0} or θ, i.e., $T(\theta, E_F)$. The overall zero-temperature conductance G can be calculated by integration of Eq. (12) over the y-component wavevector[19,45], which can be written as

$$G = \frac{2e^2}{h}\frac{W}{2\pi\hbar}\int dp_y T(p_y) = G_0 \int_{-\pi/2}^{\pi/2} d\theta \cos\theta T(\theta,E_F), \qquad (13)$$

where the factor 2 accounts for the twofold spin degeneracy, W is the transverse dimension of the interface and $G_0 = e^2 k_F W/(\pi h)$ is the unit of conductance.

It is well known that the electron spin is locked in the surface plane for a purely 2D system[6,15,16]. Naturally, it is interesting to study whether this spin-locking characteristic can be maintained in the presence of the time-periodic potential and the gate bias voltage. Based on the wavefunctions in Eqs. (8) to (10), we can calculate the spin polarization averaged over spin-space, i.e., $P_\ell(t) = \hbar/2\langle\psi|\sigma_\ell|\psi\rangle$, with $\ell = x, y, z$. The time average of the spin polarization is then defined as $\bar{P}_\ell = \omega\int_0^{2\pi/\omega} dt P_\ell(t)/2\pi$.

Numerical results and discussion

In this section, we numerically study the transport property of the topological surface states modulated by a time-dependent potential

for varying gate bias potential. We first analyze the total transmission $T(\theta, E_F)$ as a function of the electron injection-angle θ for different amplitudes and frequencies of the time-dependent potential, as shown in Fig. 2. In our numerical calculations, the following parameter values are assumed: Fermi energy of $E_F = 100$ meV, Fermi velocity of $v_F = 5 \times 10^5$ m/s, and length of central region (where the time-dependent potential is applied) of $L = 60$ nm, which provides a sufficiently thick barrier for electrons with a Fermi wave length $\lambda_F \approx 20$ nm. Under zero shift of the Dirac points in region I and III, i.e., $\mu_L = \mu_R = 0$, virtually perfect transmission ($T \approx 1$) of electrons through the time-dependent central region occurs for incidence angles $|\theta| \lesssim 70°$, (see Fig. 2 (a)). Such perfect transmission of normally incident electrons is a well-known feature of Klein tunneling of Dirac fermions[23–25]. One can understand the perfect transmission as arising from the perfect matching between the electron wavefunctions of the three different regions (see Eq. (6), (7)). In the presence of a time-dependent potential, the large-angle transmission of electron is modulated, and the modulation becomes more obvious at larger amplitude, e.g., $u_0 = 3\hbar\omega$ represented by the black curve. This phenomenon can be ascribed to the time-dependent potential, as there exists no other potential barrier over the entire surface of the device. In Fig. 2 (b), we applied gate voltage of the same sign to the left and right parts of the conducting channel, i.e., $\mu_L = \mu_R = 50$ meV. In this case, the large-angle transmission is suppressed, and electron transmission is mainly confined to a smaller range of incident angles of $|\theta| \lesssim 40°$. However, perfect transmission is still observed at normal incidence, i.e., at $\theta = 0$. The effect of the time-dependent potential on the transmission probability is relatively minor and confined to some oscillations at θ close to $40°$. When the applied gate voltage is increased, i.e., to $\mu_L = \mu_R = 200$ meV, the transmission is further confined to a smaller range of θ, as shown in Fig. 2(c). Perfect transmission, however, still persists at normal incidence.

It is interesting to note perfect transmission of normally incident electrons no longer occur when a finite gate bias voltage is applied. Even a small bias voltage, e.g., $V = 10$ meV, can result in the disappearance of the perfect normal tunneling (see Fig. 2(d).) When an electron is injected normally from region I, and transmits through the central region into the region III, the asymmetry in the gate potentials of region I and III destroys the perfect matching of the electron wavefunctions in the three regions, resulting in a finite reflection and hence imperfect transmission process. This phenomenon is a striking result in this paper. In addition, the transmission profile is slightly modulated by the time-dependent potential, especially near the threshold values of θ where there is a sharp drop in the transmission probability. The effect of the time-dependent potential becomes weaker with increasing gate bias voltage. As shown in Fig. 2(e), when $V = 100$ meV, the modulation due to the time-dependent potential is hardly visible. Next, we study the effect of the frequency of the time-dependent potential on the transmission profile. The transmission $T(\theta, E_F)$ is plotted for different frequencies with a fixed value of $u_0/\hbar\omega = 1.5$ (see Fig. 2(f)). It is observed that high-frequency potential induces a stronger modulation of the large-angle transmission, as reflected by the larger oscillations in the transmission profile.

To further analyze the effect of the time-dependent potential, we investigate the transmission probability as a function of the frequency for different amplitudes with a fixed incident angle, as shown in Fig. 3(a). Under equal gate voltage and no bias condition of $\mu_L = \mu_R = 50$ meV, the transmission shows oscillations with frequency, with the oscillatory behavior becoming more pronounced with increasing amplitude of the time-dependent potential. Next, we consider the asymmetrical case, $\mu_L = -\mu_R = 50$ meV, as shown in Fig. 3(b). As in the previous case, the time-dependent potential induces an oscillatory behavior in the transmission with respect to frequency. However, the transmission probability is significantly smaller than that in the equal voltage case, and drops to almost zero
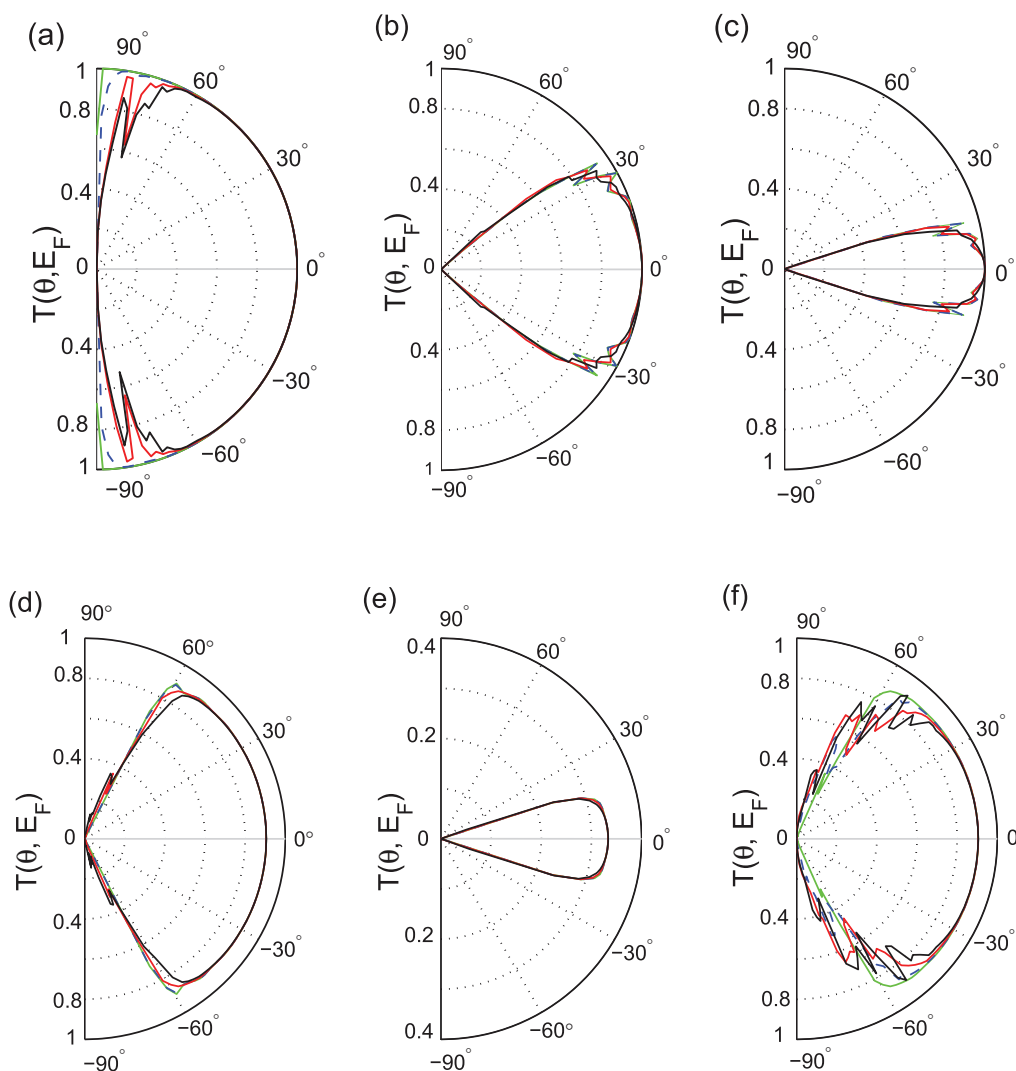
Figure 2 | The total transmission $T(\theta, E_F)$ plotted as a function of the electron injection-angle θ, for (a) $\mu_L = \mu_R = 0$, (b) 50 meV, and (c) 200 meV, for (d) $\mu_L = -\mu_R = 5$ meV, (e) $\mu_L = -\mu_R = 50$ meV. Green, blue, red and black curves correspond to $u_0 = 0, 0.5, 1.5, 3\ \hbar\omega$ with $\omega = 3.05$ THz. Especially, in the subgraph (f), $\mu_L = -\mu_R = 5$ meV, and Green, blue, red and black curves correspond to $\omega = 3.05, 6.1, 9.15, 12.2$ THz with $u_0 = 1.5\ \hbar\omega$. The Fermi energy is chosen to be $E_F = 100$ meV and the Fermi velocity is $v_F = 5 \times 10^5$ m/s.
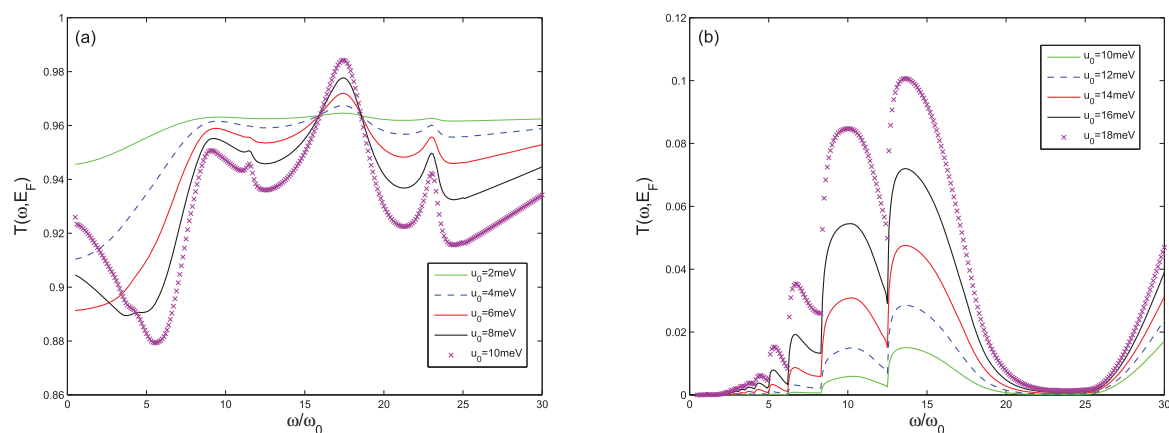

Figure 3 | **Transmission probability T as a function of the frequency of the time-dependent potential for (a) $\mu_L = \mu_R = 50$ meV and (b) $\mu_L = -\mu_R = 50$ meV.** The frequency unit ω_0 is 1.525 THz and the incident angle is $\theta = 30°$. Other parameters are the same as those in Fig. 2.
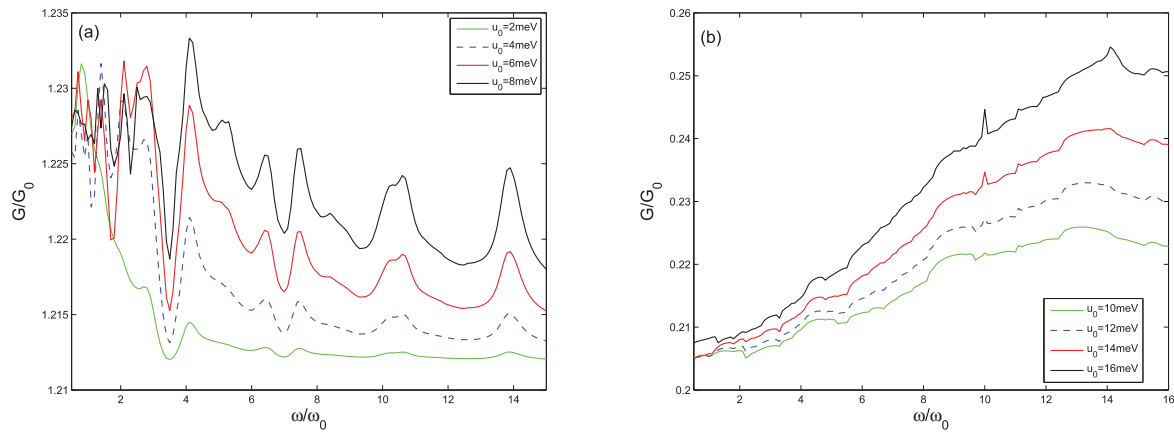
Figure 4 | The conductance G as a function of the frequency of the time-dependent potential for (a) $\mu_L = \mu_R = 50$ meV and (b) $\mu_L = -\mu_R = 50$ meV. The frequency unit ω_0 is 1.525 THz. Other parameters are the same as those in Fig. 2.

at certain range of frequencies, e.g., $21\omega_0 \lesssim \omega \lesssim 25\omega_0$. We also find that the transmission probability increases with increasing amplitude of the time-dependent potential. By contrast, in the equal-voltage case, the reverse trend occurs, i.e., the transmission probability is lowered as the potential amplitude u_0 is increased for the incident angle $\theta = 30°$. For smaller incident angles of $|\theta| < \pi/10$, the trend of increasing T with increasing u_0 remains. Since the bulk of the transmission occurs with electrons having small incident angles of $|\theta| < \pi/10$, the overall conductance increases with increasing u_0 in the equal-voltage case.

In Fig. 3, we analyze the transport behaviors only for a specific incident angle. Next, we consider the effect of the time-dependent potential on the overall zero-temperature conductance G, which comprises of contribution of all electrons incident within the angular range of $-\pi/2 \lesssim \theta \lesssim \pi/2$. In Fig. 4, G is plotted as a function of frequency ω for different potential amplitudes u_0. One can see that the conductance G is significantly higher in the equal-voltage case (Fig. 4(a)), compared to the asymmetrical case (Fig. 4(b)). However, for both cases, the conductance G increases with the potential amplitude u_0. Thus, one can surmise that time-dependent transport modes

Figure 5 | The time-averaged spin polarization $\bar{\mathbf{P}}$ plotted as a function of the electron injection-angle θ for $\omega = 3.05$ THz and $u_0 = 2\hbar\omega$. Other parameters are the same as those in Fig. 2.

(with oscillating potential in the THz frequency) can result in enhanced overall conductance, irrespective of the presence or absence of gate bias voltage.

To analyze the spin-locking characteristic of the spin polarization, we investigate the time-averaged spin polarization $\bar{\mathbf{P}} = \bar{P}_x \hat{e}_x + \bar{P}_y \hat{e}_y + \bar{P}_z \hat{e}_z$ at $x = L/2$, as a function of the electron injection-angle θ for different gate bias voltages, as shown in Fig. 5. The length of the arrows denotes the amplitude of the spin polarization, while a dot represents zero spin polarization. In the numerical calculation, the Fermi energy is set to $E_F = 100$ meV, the frequency and the amplitude are fixed to be $\omega = 3.05$ THz and $u_0 = 2\hbar\omega$. It is found that the z-component spin polarization is zero, $\bar{P}_z = 0$, i.e., the spin polarization is still locked to the x-y plane. When there is no shift of Dirac points in region I and III, i.e., $\mu_L = \mu_R = 0$, $\bar{\mathbf{P}}$ has a left-handed helicity and is always perpendicular to the wavevector $\mathbf{q}_0$ of the incident electrons. For this case, the spin polarization exists over a large angular range, $\theta \lesssim 70°$, which is consistent with the large-angle perfect transmission in Fig. 2. Under the equal-voltage case, e.g., $\mu_L = \mu_R = 50, 200$ meV, $\bar{\mathbf{P}}$ is still perpendicular to the wavevector $\mathbf{q}_0$, but the angular range of the spin polarization decreases with increasing gate potential. Thus, one can adjust the spin polarization and confine it to the small-angle region by changing the gate voltages of the left and right portions of the conducting channel. Interestingly, we also observe that the characteristic left-handed helicity of the transmitted electrons is also broken in the presence of a finite gate bias. The deviation from the helical spin orientation becomes more pronounced as the bias voltage is increased (as can be observed by the green arrows corresponding to the largest applied bias). In addition, we found that the deviation from the left-handed helicity is greater for large-angle transmission. For the zero-angle transmission, the spin polarization is robust with respect to the applied bias voltage and time-dependent potential. In terms of the definition of the spin polarization, when $\theta = 0°$, we find that $P_{x/y}(t) \propto \sum_{m,m'} t_m^*(\varepsilon) t_{m'}(\varepsilon') f_m [\gamma_{0,R}(\varepsilon + m'\hbar\omega) \mp \gamma_{0,R}(\varepsilon + m\hbar\omega)]$, where f_m is an exponential function including m and m'. Basically, the condition $\gamma_{0,R}(\varepsilon + m'\hbar\omega) - \gamma_{0,R}(\varepsilon + m\hbar\omega) = 0$ can be satisfied for the small values of m and m' in the above five cases, while the transmission coefficients t_m will become zero for larger values of m. Thus for the special case of $\theta = 0°$, $P_x(t)$ becomes zero and this results in the robustness of the spin polarization.
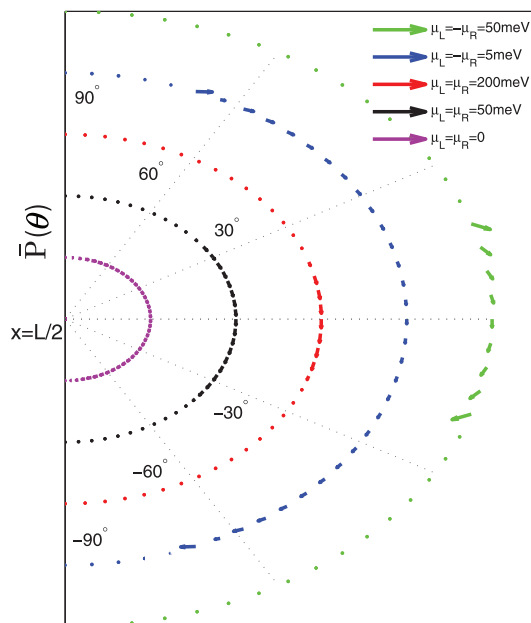
Summary

In the above, we present a theoretical study of the influence of time-dependent potential and gate bias voltage on the chiral tunneling for topological surface states. Utilizing the scattering matrix method, we numerical analyze the effect of the time-dependent potential on the

transmission probability, the conductance and the spin polarization. We find that, under the equal-voltage case (where the gate potentials of region *I* and *III* are identical), perfect transmission occurs for electrons which are injected normally to the interfaces. The spin polarization retains its left-handed helicity, but the angle range of the spin polarization decrease with increasing gate voltage. However, in the presence of an asymmetrical gate voltage two signature characteristics of Klein tunneling no longer hold. Firstly, normally incident electrons no longer experience perfect transmission-the transmission probability of such electrons diminishes with increasing gate bias voltage. Secondly, the left-handed helicity of the spin polarization of transmitted electrons is also broken by the finite gate bias. As for the time-dependent potential, its influence is prominent only for large-angle transmission, where it induces oscillatory or resonance-like behavior in the transmission. The overall conductance of the device is significantly reduced upon application of a gate bias voltage. Finally, the presence of time-dependent transport modes which give rise to time-dependent potential, would enhance the device conductance, irrespective of the presence or absence of gate bias voltage.

1. Hasan, M. Z. & Kane, C. L. Colloquium: Topological insulators. *Rev. Mod. Phys.* **82**, 3045–3067 (2010).
2. Qi, X. L. & Zhang, S. C. Topological insulators and superconductors. *Rev. Mod. Phys.* **83**, 1057–1110 (2011).
3. Zhang, H. J. *et al.* Topological insulators in Bi_2Se_3, Bi_2Te_3 and Sb_2Te_3 with a single Dirac cone on the surface. *Nat. Phys.* **5**, 438–442 (2009).
4. Bardarson, J. H., Brouwer, P. W. & Moore, J. E. Aharonov-Bohm Oscillations in Disordered Topological Insulator Nanowires. *Phys. Rev. Lett.* **105**, 156803 (2010).
5. Xiu, F. *et al.* Manipulating surface states in topological insulator nanoribbons. *Nat. Nanotechnol.* **6**, 216–221 (2011).
6. Zhu, J. J., Yao, D. X., Zhang, S. C. & Chang, K. Electrically Controllable Surface Magnetism on the Surface of Topological Insulators. *Phys. Rev. Lett.* **106**, 097201 (2011).
7. Fujita, T., Jalil, M. B. A. & Tan, S. G. Topological Insulator Cell for Memory and Magnetic Sensor Applications. *Appl. Phys. Express* **4**, 094201 (2011).
8. Tang, H., Liang, D., Qiu, R. L. J. & Gao, X. P. A. Two-Dimensional Transport-Induced Linear Magneto-Resistance in Topological Insulator Bi_2Se_3 Nanoribbons. *ACS Nano* **5**, 7510–7516 (2011).
9. Li, Y. *et al.* Magnetoresistive effect of a topological-insulator waveguide in the presence of a magnetic field. *Appl. Phys. Lett.* **101**, 262403 (2012).
10. Hsieh, D. *et al.* A tunable topological insulator in the spin helical Dirac transport regime. *Nature* **460**, 1101–1106 (2009).
11. Kitaev, A. Yu. Fault-tolerant quantum computation by anyons. *Ann. Phys.* **303**, 2–30 (2003).
12. Fu, L. & Kane, C. L. Superconducting Proximity Effect and Majorana Fermions at the Surface of a Topological Insulator. *Phys. Rev. Lett.* **100**, 096407 (2008).
13. Peng, H. *et al.* Aharonov-Bohm interference in topological insulator nanoribbons. *Nature Mater.* **9**, 225–229 (2010).
14. Li, W., Zang, J. D. & Jiang, Y. J. Size effects on transport properties in topological Anderson insulators. *Phys. Rev. B* **84**, 033409 (2011).
15. Yokoyama, T., Zang, J. D. & Nagaosa, N. Theoretical study of the dynamics of magnetization on the topological surface. *Phys. Rev. B* **81**, 241410(R) (2010).
16. Kong, B. D., Semenov, Y. G., Krowne, C. M. & Kim, K. W. Unusual magnetoresistance in a topological insulator with a single ferromagnetic barrier. *Appl. Phys. Lett.* **98**, 243112 (2011).
17. Hao, L., Thalmeier, P. & Lee, T. K. Topological insulator ribbon: Surface states and dynamical response. *Phys. Rev. B* **84**, 235303 (2011).
18. Liu, G. H., Zhou, G. H. & Chen, Y. H. Modulation of external electric field on surface states of topological insulator Bi_2Se_3 thin films. *Appl. Phys. Lett.* **101**, 223109 (2012).
19. Beenakker, C. W. J. Colloquium: Andreev reflection and Klein tunneling in graphene. *Rev. Mod. Phys.* **80**, 1337–1354 (2008).
20. Castro Neto, A. H., Peres, N. M. R., Novoselov, K. S. & Geim, A. K. The electronic properties of graphene. *Rev. Mod. Phys.* **81**, 109–162 (2009).
21. Das Sarma, S., Adam, S., Hwang, E. & Rossi, E. Electronic transport in two-dimensional graphene. *Rev. Mod. Phys.* **83**, 407–470 (2011).
22. Zeb, M. A., Sabeeh, K. & Tahir, M. Chiral tunneling through a time-periodic potential in monolayer graphene. *Phys. Rev. B* **78**, 165420 (2008).
23. Katsnelson, M. I., Novoselov, K. S. & Geim, A. K. Chiral tunnelling and the Klein paradox in graphene. *Nat. Phys.* **2**, 620–625 (2006).
24. He, W. Y., Chu, Z. D. & He, L. Chiral Tunneling in a Twisted Graphene Bilayer. *Phys. Rev. Lett.* **111**, 066803 (2013).
25. Bala Kumar, S. & Guo, J. Chiral tunneling in trilayer graphene. *Appl. Phys. Lett.* **100**, 163102 (2012).
26. Katsnelson, M. I. & Novoselov, K. S. Graphene: New bridge between condensed matter physics and quantum electrodynamics. *Solid State Commun.* **143**, 3–13 (2007).
27. Vozmediano, M. A. H., Katsnelson, M. I. & Guinea, F. Gauge fields in graphene. *Phys. Rep.* **496**, 109–148 (2010).
28. Zhang, X., Wang, J. & Zhang, S. C. Topological insulators for high-performance terahertz to infrared applications. *Phys. Rev. B* **82**, 245107 (2010).
29. Kitagawa, T. *et al.* Transport properties of nonequilibrium systems under the application of light: Photoinduced quantum Hall insulators without Landau levels. *Phys. Rev. B* **84**, 235108 (2011).
30. Dóra, B., Cayssol, J., Simon, F. & Moessner, R. Optically Engineering the Topological Properties of a Spin Hall Insulator. *Phys. Rev. Lett.* **108**, 056602 (2012).
31. Wang, Z. G., Fu, Z. G. & Zhang, P. Magnetoexcitons and optical absorption of bilayerstructured topological insulators. *Appl. Phys. Lett.* **100**, 161602 (2012).
32. Junck, A., Refael, G. & von Oppen, F. Photocurrent response of topological insulator surface states. *Phys. Rev. B* **88**, 075144 (2013).
33. Katan, Y. T. & Podolsky, D. Modulated Floquet Topological Insulators. *Phys. Rev. Lett.* **110**, 016802 (2013).
34. Lindner, N. H., Refael, G. & Galitski, V. Floquet topological insulator in semiconductor quantum wells. *Nat. Phys.* **7**, 490–495 (2011).
35. Inoue, J. I. & Tanaka, A. Photoinduced Transition between Conventional and Topological Insulators in Two-Dimensional Electronic Systems. *Phys. Rev. Lett.* **105**, 017401 (2010).
36. Wang, Y. H., Steinberg, H., Jarillo-Herrero, P. & Gedik, N. Observation of Floquet-Bloch States on the Surface of a Topological Insulator. *Science* **342**, 453–457 (2013).
37. Wang, Y. *et al.* Gate-Controlled Surface Conduction in Na-Doped Bi_2Te_3 Topological Insulator Nanoplates. *Nano Lett.* **12**, 1170 (2012).
38. Liu, H. & Ye Peide, D. Atomic-layer-deposited Al_2O_3 on Bi_2Te_3 for topological insulator field-effect transistors. *Appl. Phys. Lett.* **99**, 052108 (2011).
39. Ryzhii, V., Ryzhii, M., Satou, A., Otsuji, T. & Kirova, N. Device model for graphene bilayer field-effect transistor. *J. Appl. Phys.* **105**, 104510 (2009).
40. Hu, G. X. *et al.* Quasi-Ballistic Transport Model for Graphene Field-Effect Transistor. *IEEE Trans. Electron Devices* **60**, 2410 (2013).
41. Trauzettel, B., Blanter, Y. M. & Morpurgo, A. F. Photon-assisted electron transport in graphene: Scattering theory analysis. *Phys. Rev. B* **75**, 035305 (2007).
42. Büttiker, M. Four-Terminal Phase-Coherent Conductance. *Phys. Rev. Lett.* **57**, 1761 (1986).
43. Landauer, R. Conductance determined by transmission: probes and quantized constriction resistance. *J. Phys.: Condens. Matter* **1**, 8099–8110 (1989).
44. Datta, S. Electronic Transport in Mesoscopic System (Cambridge University Press, Cambridge, 1995).
45. Cheianov, Vadim, V. & Fal'ko, Vladimir, I. Selective transmission of Dirac electrons and ballistic magnetoresistance of n-p junctions in graphene. *Phys. Rev. B* **74**, 041403(R) (2006).

Acknowledgments

Author contributions

Y.L. conceived the idea and contributed to the theoretical analysis and interpretation of data, and wrote the manuscript. M.B.A.J. and G.H.Z. contributed to the interpretation of the numerical results and contributed to the writing of the manuscript. W.Z. and S.G.Tan contributed in the discussion. R.B. participated in the numerical calculation. All authors reviewed the manuscript.

Additional information